Disorder-Driven Multifractality Transition in Weyl Nodal Loops

Miguel Gonçalves,[1] Pedro Ribeiro,[1,2] Eduardo V. Castro,[3,2] and Miguel A. N. Araújo[1,4,2]
[1]CeFEMA, Instituto Superior Técnico, Universidade de Lisboa, Av. Rovisco Pais, 1049-001 Lisboa, Portugal
[2]Beijing Computational Science Research Center, Beijing 100084, China
[3]Centro de Física das Universidades do Minho e Porto, Departamento de Física e Astronomia, Faculdade de Ciências, Universidade do Porto, 4169-007 Porto, Portugal
[4]Departamento de Física, Universidade de Évora, P-7000-671 Évora, Portugal

(Received 23 August 2019; accepted 10 March 2020; published 1 April 2020)

The effect of short-range disorder in nodal line semimetals is studied by numerically exact means. For arbitrary small disorder, a novel semimetallic phase is unveiled for which the momentum-space amplitude of the ground-state wave function is concentrated around the nodal line and follows a multifractal distribution. At a critical disorder strength, a semimetal to compressible metal transition occurs, coinciding with a multi- to single-fractality transition. The universality class of this critical point is characterized by the correlation length and dynamical exponents. At considerably higher disorder, an Anderson metal-insulator transition takes place. Our results show that the nature of the semimetallic phase in nonclean samples is fundamentally different from a clean nodal semimetal.

DOI: 10.1103/PhysRevLett.124.136405

The robustness of certain material properties to perturbations is arguably the most appealing property of topological matter. Topological insulators stood out as an important class of topological materials [1,2] whose stability with respect to interactions and disorder is by now fairly well established [3,4]. Gapless systems can, however, also support nontrivial momentum-space topology and are expected to be less robust to such effects. Among these, are the Weyl nodal loop (WNL) semimetals, for which the valence and conduction bands linearly touch along one-dimensional (1D) loops in the three-dimensional (3D) momentum space [5]. Their recent theoretical prediction [6–8] and experimental discovery [9,10] triggered intense experimental [11–20] and theoretical interest [21–34].

A manifestation of WNL's topological nature is the presence of surface ("drumhead") edge states [7,24,35–37] on surfaces parallel to the loop plane, which are induced by chiral symmetry. Since the Fermi surface is reduced to a 1D nodal line, the density of states (DOS), $\rho(E)$, vanishes linearly for low energies, i.e., $\rho(E) \propto |E|$.

The robustness of the topological semimetal state to interactions [38–42] and disorder [43,44] is of major importance to understand in which conditions it might be observed. For Dirac and Weyl systems with isolated nodal points, the effect of static disorder has recently been addressed by a series of thorough numerical studies [45–50]. The clean-limit incompressible semimetallic state was shown to survive up to a finite critical strength of a box-distributed disorder potential where a transition to a compressible diffusive metal takes place [51].

For a WNL, the exact nature of the finite disorder state is yet unknown. Coulomb interactions were shown to induce a quasiparticle lifetime, thus yielding Fermi liquid behavior [52]. Weak disorder does not change the compressibility, to leading order [53]. Nevertheless, disorder, with or without interactions, was found to be marginally relevant in the clean case [53], pointing to a different scenario than nodal point semimetals. Perturbative arguments are, however, of limited use to characterize the stable fixed point at finite disorder. The latter is of key importance to understand the properties of WNL compounds, particularly regarding transport, which has, up to know, been assumed diffusive [54].

In this Letter, we unveil the phase diagram of a WNL in the presence of short-range disorder using numerically exact methods. It includes a novel multifractal (MF) semimetallic (SM) phase, corresponding to the stable fixed point for weak disorder. Our main results are summarized in Fig. 1. We show that any small amount of disorder mixes all the Weyl states along the nodal line depicted in Fig. 1(a), and that the width of the wave function Γ vanishes with increasing linear system size L. The resulting state is fundamentally different from the clean one. Although the DOS still vanishes at the Fermi level, i.e., $\rho_0 \equiv \rho(E = 0) = 0$, the momentum-space wave function has a multifractal structure. The MF-SM phase survives up to a critical disorder strength, where a transition to a single-fractal (SF) metallic (M) phase takes place. In this phase the system is a standard diffusive metal with a finite ρ_0 and Γ loses system size dependence. At larger disorder strength, an Anderson metal-insulator transition occurs. The phase diagram is sketched in Fig. 1(b).

Model and methods.—We study a two-band model of a WNL on a cubic lattice with short-range disorder,

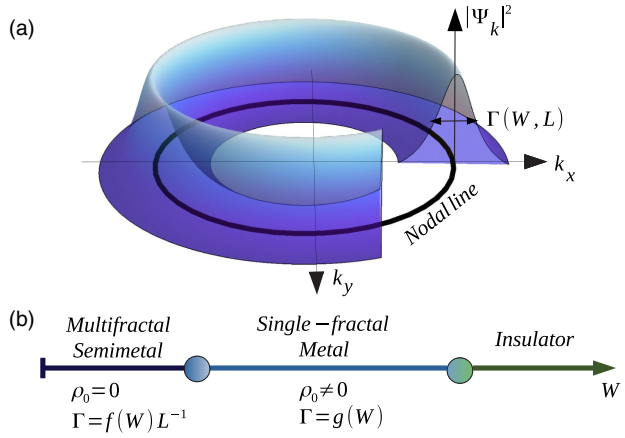

FIG. 1. (a) The Fermi surface of the WNL is a continuous line in the plane $k_z = 0$. The ground-state wave function has a width $\Gamma(W, L)$ around the loop, for fixed linear system size (L) and disorder strength (W). (b) Schematic phase diagram as a function of W. For small W, the DOS at $E = 0$ vanishes, $\rho_0 = 0$, and Γ vanishes with L^{-1}—the system is in a multifractal semimetallic phase. For W larger than a critical disorder strength, $\rho_0 \neq 0$ and Γ is L independent—the system enters a single-fractal metallic phase. For larger W the system becomes an Anderson insulator.

$$H = \sum_{\boldsymbol{k}} c^{\dagger}_{\boldsymbol{k}} H_{\boldsymbol{k}} c_{\boldsymbol{k}} + \sum_{\boldsymbol{r}} c^{\dagger}_{\boldsymbol{r}} V_{\boldsymbol{r}}(W) c_{\boldsymbol{r}}. \quad (1)$$

The first term describes a clean WNL, with $\boldsymbol{k}$ a 3D Bloch vector, $H_{\boldsymbol{k}} = [t_x \cos(k_x) + t_y \cos(k_y) + \cos(k_z) - m]\tau_x + t_2 \sin(k_z)\tau_y$, with τ_x, τ_y Pauli matrices acting on the orbital pseudospin indices $\alpha = 1, 2$, and $c^{\dagger}_{\boldsymbol{k}} = (c^{\dagger}_{\boldsymbol{k},1} c^{\dagger}_{\boldsymbol{k},2})$. The second term is the disorder potential, where $\boldsymbol{r}$ is a lattice site and $V_{\boldsymbol{r}}(W) = \mathrm{diag}(v_{\boldsymbol{r}1}, v_{\boldsymbol{r}2})$, with random variables $v_{\boldsymbol{r}\alpha} \in [-W/2, W/2]$. The results presented hereafter are for $t_x = 1.1$, $t_y = 0.9$, $m = 2.12$, and $t_2 = 0.8$. This choice yields a single nodal line, arising for $k_z = 0$. The hopping anisotropy breaks unwanted degeneracies and ensures the system is generic within this class.

We numerically characterize the spectral and wave function properties. To compute the DOS we use the kernel polynomial method (KPM) with an expansion in Chebyshev polynomials to order N_m [55–57], reaching system sizes up to $L = 10^3$. To characterize the system's lowest energy eigenstates, we use Lanczos exact diagonalization (ED).

The eigenstates' structure is revealed by the generalized momentum-space inverse participation ratio [58,59],

$$\mathcal{I}_k(q) = \left(\sum_{\boldsymbol{k},\alpha} |\Psi_{\boldsymbol{k},\alpha}|^2 \right)^{-q} \sum_{\boldsymbol{k},\alpha} |\Psi_{\boldsymbol{k},\alpha}|^{2q} \propto L^{-\tau_k(q)}, \quad (2)$$

where $\Psi_{\boldsymbol{k},\alpha}$ is the eigenstate amplitude in the $\boldsymbol{k}$ Bloch momentum state and orbital α. The size dependence is characterized by a q-dependent exponent τ_k, defined in terms of the generalized dimension, $D_k(q)$, as $\tau_k(q) = D_k(q)(q-1)$. In a ballistic phase, the wave function is localized in momentum space, $\mathcal{I}_k(q)$ is L independent, and $D_k(q) = 0$ for $q > 0$. For a 3D-diffusive metal or an Anderson insulator, $D_k(q) = 3$. In these cases $D_k(q)$ is constant, and the system is a single fractal. Multifractals correspond to cases where $D_k(q)$ is q dependent. This happens, for instance, for the real-space inverse participation ratio at a disorder driven metal-insulator transition [60].

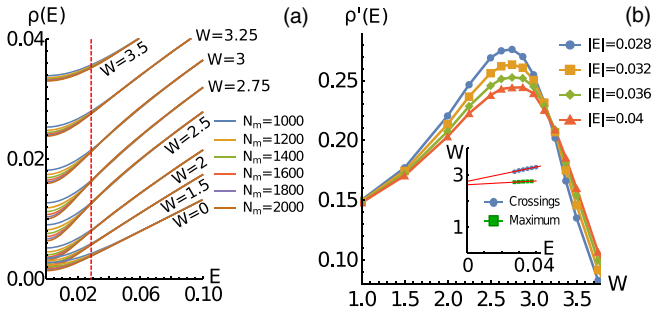

FIG. 2. (a) DOS for different W and varying N_m. For energies above the dashed vertical line, differences between $N_m = 1000$ and $N_m = 2000$ are below 1%. (b) $\rho'(E)$, converged with N_m, as a function of W, for different E. Inset: Extrapolation to $E \to 0$ of $\rho'(E)$ crossing points (Filled circle) and $\rho'(E)$ maximum (Filled square).

To attenuate finite-size effects, we use twisted boundary conditions and compute $\mathcal{I}_k$ averaging over random twist angles, disorder, and the two lowest energy eigenstates, taking 250–1000 configurations. τ_k is extracted from the size dependence of $\mathcal{I}_k$.

SM-M transition.—The DOS for different W values and varying N_m is shown in Fig. 2(a) [note that $\rho(E) = \rho(-E)$]. For large enough $|E|$, $\rho(E)$ converges for the highest N_m attainable. However, within an energy window around $E = 0$, $\rho(E)$ does not converge for the largest N_m. This difficulty of the KPM method in resolving sharp spectral features arises already in the clean limit and prevents a direct determination of ρ_0 for small W. Nonetheless, for larger W the system is clearly metallic as ρ_0 converges to a finite value.

Quantitative predictions can be obtained from $\partial\rho/\partial E \equiv \rho'(E)$ as a function of W, plotted for different energies within the converged region in Fig. 2(b). $\rho'(E)$ increases up to a maximum value at $W = W_{\max}(E)$ and decreases abruptly for larger W. Thus, there are two different regimes when $E \to 0$: for smaller (larger) W, $\rho'(E)$ increases (decreases) until reaching $\rho'(0) \neq 0$ [$\rho'(0) = 0$]. These results strongly suggest the transition value, W_c, from a semimetal ($\rho_0 = 0$) into a metal ($\rho_0 \neq 0$) to be finite. In the SM phase, the growth of $\rho'(E)$ as $E \to 0$ agrees with the observed negative concavity of $\rho(E)$ [see Fig. 2(a)], corroborating the $\rho_0 \to 0$ behavior. This provides two ways to compute W_c: (i) Using $\lim_{E\to 0} W_{\max}(E) = W_c$, and extrapolating $W_{\max}(E \to 0)$ from the converged region,

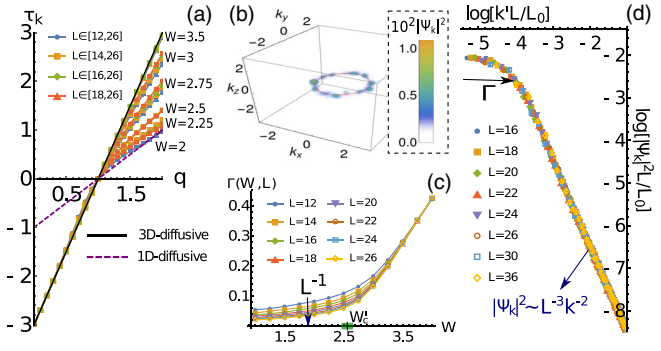

FIG. 3. (a) Exponent $\tau_k(q)$ vs q [see Eq. (2)] for different W and L. (b) Plot of the ground-state PD in momentum space $|\Psi_{\boldsymbol{k}}|^2$ for a configuration with $W = 3.5$. (c) $|\Psi_{\boldsymbol{k}}|^2$ width around the loop $\Gamma(W, L)$ vs W for varying L. (d) $|\Psi_{\boldsymbol{k}}|^2$ as a function of k' for $W = 1.75$ and $k_z = 0$, where k' is measured relative to the loop. The system is in the MF regime and the PD curves collapse by rescaling $|\Psi_{\boldsymbol{k}}|^2 \to |\Psi_{\boldsymbol{k}}|^2 L$ and $k' \to k'L$. $L_0 = 16$ is the smallest used linear system size.

which yields $W_c = 2.61 \pm 0.01$ [inset of Fig. 2(b)]; (ii) the crossing point $W_{\mathrm{Cross}}(E, \Omega)$, for which $\rho'(E) = \rho'(\Omega E)$ with $\Omega > 0$, obeys $\lim_{E\to 0} W_{\mathrm{Cross}}(E, \Omega) = W_c$. By computing the crossing point, $W_{\mathrm{Cross}}(E, \Omega)$, between $\rho'(E)$ and $\rho'(\Omega E)$ for different E in the converged region ($\Omega \simeq 0.9$), we obtained a linear dependence on E. Extrapolating $E \to 0$ through a linear fit, yields $W_c = 2.74 \pm 0.02$ [Fig. 2(b), inset].

These two methods should yield the same result when $E \to 0$. However, there is an extrapolating uncertainty in the results due to the bounded lowest attainable energy. We estimate the critical point by computing the least squares between the two, yielding $W_c = 2.64 \pm 0.05$, compatible with the results obtained with ED [61].

In contrast with the numerical exact method, the self-consistent Born approximation yields an exponentially suppressed DOS for low disorder [61], similar to 3D Weyl semimetals [66].

MF-SF transition.—We now discuss the differences between the MF and SF regimes. The computed exponent $\tau_k(q)$ is shown in Fig. 3(a) [67]. A very peculiar behavior can be observed in the MF phase: for $q < 1$, $D_k(q) = 3$, as expected for a 3D-diffusive metal; whereas for $q > 1$, $D_k(q) = 1$, implying $\boldsymbol{k}$-space delocalization in one dimension. The origin of this phenomenon is discussed below. In the SF case, for larger W, $\tau_k(q)$ follows the 3D-diffusive line [Fig. 3(a)] corresponding to $D_k(q) = 3$. A finite-size scaling analysis shows that $\tau_k(q)$ decreases (increases) with L for $W < 2.25$ ($W > 2.75$), demonstrating the multi (single)-fractal nature of this phase in the thermodynamic limit. By inspection, the critical point where the MF-SF transition occurs is thus within $W_c' \in]2.25, 2.75[$. Below, we compute W_c' and show it is compatible with W_c, obtained for the semimetal-metal transition.

The origin of the MF-SF transition can be understood by inspecting the probability distribution (PD) of the lowest energy eigenstate in momentum space, $|\Psi_{\boldsymbol{k}}|^2$. As shown in Fig. 1(b) for a typical realization of disorder, the PD is concentrated along a region of width Γ along the nodal line. Let Σ_{loop} be the set of $(\boldsymbol{k}, \alpha)$ points inside a torus with minor radius Γ surrounding the WNL. Since the loop is approximately circular, the number of points in Σ_{loop} can be estimated as $N \simeq 2\pi\Gamma^2 P L^3/(2\pi)^3$, where P is the loop perimeter. Since N can also be estimated from $\mathcal{I}_k \equiv \mathcal{I}_k(q = 2) \simeq 1/N$, we define the width of the wave function's PD to be

$$\Gamma = \frac{2\pi}{\sqrt{\mathcal{I}_k L^3 P}}. \tag{3}$$

Figure 3(c) depicts Γ as a function of W and L [68]. We found that $\Gamma(W, L)$ converges with system size in the SF phase and scales to zero with L^{-1} in the MF phase.

Within the MF phase, a scaling analysis of $|\Psi_{\boldsymbol{k}}|^2$ in the plane $k_z = 0$ is shown in Fig. 3(d). The rescalings $|\Psi_{\boldsymbol{k}}|^2 \to |\Psi_{\boldsymbol{k}}|^2 L$ and $k' \to k'L$, where k' is the toroidal minor radial coordinate, make the numerical results for different L collapse. This shows that, in this regime, momentum space can be divided in two regions: $k' < \Gamma$, where $|\Psi_{\boldsymbol{k}}|^2 \sim L^{-1}(k')^0$, and $k' > \Gamma$, where the PD decays with k' as $|\Psi_{\boldsymbol{k}}|^2 \sim L^{-3}(k')^{-2}$. An estimation of $\mathcal{I}_k(q)$ yields, in the large L limit, $\mathcal{I}_k(q) = c_1 \sum_{\boldsymbol{k}\in\Sigma_{\mathrm{loop}}} L^{-q} + c_2 \sum_{\boldsymbol{k}\neq\Sigma_{\mathrm{loop}}} L^{-3q}(k')^{-2q} = c_1' L^{1-q} + c_2' L^{3(1-q)}$, where c_1, c_2, c_1', c_2' are L-independent constants. This explains the results of $\tau_k(q)$ in Fig. 3(a) as the scalings $L^{3(1-q)}$ and L^{1-q}, respectively dominate for $q < 1$ and $q > 1$. In simple words, although the larger fraction of the wave function's PD collapses in the nodal line, there is still a finite fraction that spreads over the rest of the Brillouin zone's volume. In the SF phase, while the asymptotic behavior $|\Psi_{\boldsymbol{k}}|^2 \sim L^{-3}k'^{-2}$ is also observed, the scaling collapse is obtained for $|\Psi_{\boldsymbol{k}}|^2 \to |\Psi_{\boldsymbol{k}}|^2 L^3$ [61].

It is worth noting that, as defined in Eq. (3), Γ can be numerically resolved only if $\Gamma \gg 2\pi/L$. However, when restricted to the plane $k_z = 0$, $|\Psi_{\boldsymbol{k}}|^2$ is still delocalized along the loop if the area of Σ_{loop} restricted to $k_z = 0$, i.e., ΓP is much larger than the area of the momentum-space cell $(2\pi/L)^2$. This extends the resolution computed within the $k_z = 0$ plane to $\Gamma \gg (2\pi/L)^2/P$, and allows us to study cases with $\Gamma \leq 2\pi/L$ in Fig. 3(d). For small $W(\lesssim 1.5)$, we start observing $\Gamma \sim L^{-x}$, with $1 < x < 2$, that we attribute to a lack of resolution for the available sizes [61].

To estimate the critical disorder strength, W_c', of the MF-SF transition, we define characteristic scales that are finite within the respective phases in the thermodynamic limit, and diverge at W_c'. In the MF phase, we define $\lambda_s \equiv \Gamma L P$, which diverges as $W \to W_c'^-$; in the SF phase, $\lambda_m \equiv \Gamma^{-1}$ diverges as $W \to W_c'^+$. Then, the quantity

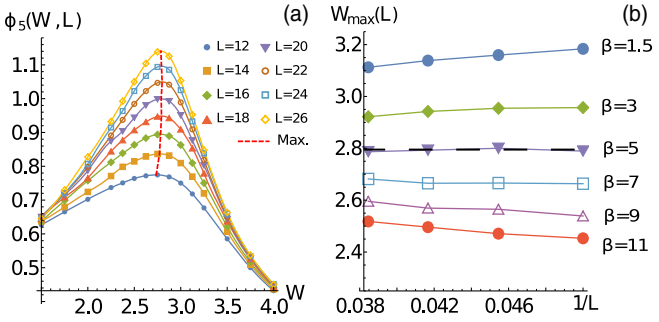

FIG. 4. (a) The quantity $\phi_\beta(W,L)$ vs W (see text), for $\beta = 5$ and varying L. The red dashed line intersects the maxima of each L curve. (b) $W_{\max}(L)$ vs L for different β, with $L \in [20, 26]$. The horizontal dashed, black line separates regimes where $W_{\max}(L)$ either increases or decreases with L.

$\phi_\beta(W,L) = (\lambda_s^{-1} + \beta\lambda_m^{-1})^{-1}$, with β a positive real constant, only diverges at $W = W_c'$. Figure 4(a) shows $\phi_\beta(W,L)$ as a function of L, for $\beta = 5$ and different L. For a fixed L, $\phi_\beta(W,L)$ has a maximum at $W = W_{\max}(L,\beta)$. The critical disorder strength can thus be obtained by $\lim_{L\to\infty} W_{\max}(L,\beta) = W_c'$, for any $\beta > 0$. However, for finite L we observe a β dependence of $W_{\max}(L,\beta)$. As shown in Fig. 4(b), there are two regimes: for $\beta < \beta_c \simeq 5$ ($\beta > \beta_c$) $W_{\max}(L,\beta)$ decreases (increases) with L. Thus, $W_{\max}(L,\beta_c)$ provides an estimation of W_c' that minimizes finite-size effects. For $L \in [20, 26]$ we find $\beta_c \approx 5$, while for smaller system sizes, $L \in [12, 18]$, $\beta_c \approx 3.6$. Extrapolating β_c for $L \to \infty$, we obtain $W_c' = 2.56 \pm 0.10$ [61], in good agreement with the critical value for the SM-M transition. In the following, we take the average value of the SM-M and MF-SF critical points and set $W_c = W_c' = 2.6 \pm 0.1$.

Scaling analysis.—We take Γ and Γ^{-1}/L as finite-size scaling variables for the SM and M phases, respectively, and write

$$\Gamma = f_s(L/\xi_s), \tag{4}$$

$$\Gamma^{-1}/L = f_m(L/\xi_m), \tag{5}$$

where f_s and f_m are, respectively, scaling functions in the SM and M phases. The thermodynamic-limit correlation lengths ξ_s and ξ_m, respectively, in the SM and M phases, scale as ξ_s, $\xi_m \sim \delta^{-\nu}$ with $\delta = |W - W_c|/W_c$. Collapsing the curves in Eq. (5) for different W, allows the determination of ξ_s and ξ_m up to multiplicative constants. The data collapse is depicted in Figs. 5(a)–5(b). Fitting $\xi_m \sim \delta^{-\nu}$ yields $\nu = 1.0 \pm 0.2$. We could not unambiguously fit ν from ξ_s due to the large error in its computation, arising from small W resolution problems (discussed before) and finite-size effects for W near W_c. Nonetheless, the value of ν obtained from ξ_s is compatible with the scaling collapse of ξ_m [61].

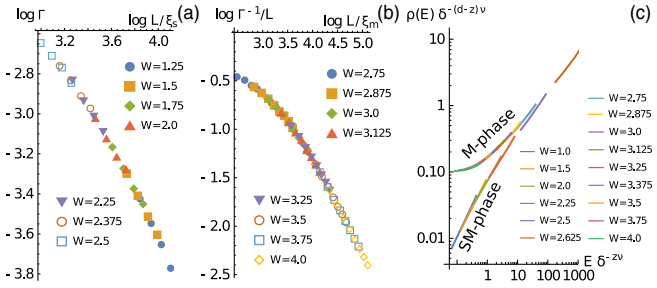

FIG. 5. (a) Collapse of scaling variable Γ by shifts of $\log \xi_s$, for $L \in [20, 26]$. (b) Collapse of scaling variable Γ^{-1}/L by shifts of $\log \xi_m$, for $L \in [12, 26]$. (c) Collapse of the $\rho(E)$ curves according to Eq. (6), obtained for different W and $E \in [0.025, 0.175]$, with parameters $\nu = 1$, $z = 1.9$ and $W_c = 2.6$. The curves collapse in two different branches that connect at $W = W_c$, corresponding to the SM and M phases.

Following Ref. [50], we assume the scaling form of the DOS near the SM-M transition to be [61]

$$\rho(E) \sim \delta^{\nu(d-z)} \mathcal{F}_\gamma(\delta^{-\nu z}|E|), \tag{6}$$

where the subscript γ in Eq. (6) distinguishes the scaling functions in the SM ($\mathcal{F}_s$) and M ($\mathcal{F}_m$) phases. At the transition, $W = W_c$, the DOS varies as $\rho(E) \sim |E|^{(d/z)-1}$. After fitting $\rho(E)$ near $W = W_c$, we obtained $z = 1.9 \pm 0.1$. This value is compatible with the results obtained with ED [61]. Using the values of z and ν determined previously, the $\rho(E)$ data collapse into two different branches (SM and M phases) touching at $W = W_c$, as shown in Fig. 5(c).

As expected, the critical exponents obtained here differ from those of the 3D metal-insulator Anderson transition [69–72], as well as from those of a disordered Weyl semimetal ($z \approx 1.5$ and $\nu \approx 1$) [50], confirming that this transition belongs to a different universality class.

Anderson transition.—In the M phase, upon increasing W, a second phase transition takes place at $W_c^l = 11.0 \pm 0.2$ [61]. The critical exponent ν is compatible with a 3D Anderson transition in the orthogonal symmetry class, between a 3D-diffusive metal and an Anderson insulator.

Discussion.—A clean WNL is unstable to an infinitesimal amount of disorder and flows to a strong-coupling fixed point, a novel phase—here dubbed multifractal-semimetal—where the DOS vanishes at the Fermi energy and the momentum-space distribution of low energy states has a multifractal structure, being concentrated on the nodal line. Upon increasing the disorder strength, the DOS becomes finite and the eigenstate's momentum-space distribution transitions to that of a 3D-diffusive metal. Both phenomena arise for the same critical value of disorder W_c, up to numerical accuracy. The ensuing multifractal semimetal to single-fractal metal phase transition belongs to a novel universality class characterized by the critical exponents, $\nu = 1.0 \pm 0.2$ and $z = 1.9 \pm 0.1$, and by the scaling

functions for the DOS and correlation lengths. Further increasing the disorder, the 3D-diffusive metal transitions to an insulating state through an Anderson metal-insulator transition.

The implications of our results to edge state physics and to the transport properties of the disordered WNL will be given elsewhere [73]. It would also be interesting to see if the rare regions effects reported for Dirac and Weyl semimetals do produce a finite contribution to ρ_0 [47,74–76] in WNL or otherwise leave the semimetallic phase unchanged [48].

We acknowledge partial support from Fundação para a Ciência e Tecnologia (Portugal) through Grants No. UID/CTM/04540/2013, and UID/CTM/04540/2019. P. R. acknowledges further support through the Investigador Contract No. IF/00347/2014. E. V. C. acknowledges partial support from FCT-Portugal through Grant No. UID/FIS/04650/2019. M. G. acknowledges further support through the Grants No. IF/00347/2014/CP1214/CT0002, No. UID/CTM/04540/2020, and No. 1018P.02595.1.01 - ACTIV ID. The hospitality of the Computational Science Research Center, Beijing, China, where the final stage of this work was carried out, is also acknowledged.

[1] M. Z. Hasan and C. L. Kane, Rev. Mod. Phys. **82**, 3045 (2010).
[2] X.-L. Qi and S.-C. Zhang, Rev. Mod. Phys. **83**, 1057 (2011).
[3] C. K. Chiu, J. C. Y. Teo, A. P. Schnyder, and S. Ryu, Rev. Mod. Phys. **88**, 035005 (2016).
[4] S. Rachel, Rep. Prog. Phys. **81**, 116501 (2018).
[5] N. P. Armitage, E. J. Mele, and A. Vishwanath, Rev. Mod. Phys. **90**, 015001 (2018).
[6] Y. Kim, B. J. Wieder, C. L. Kane, and A. M. Rappe, Phys. Rev. Lett. **115**, 036806 (2015).
[7] H. Weng, Y. Liang, Q. Xu, R. Yu, Z. Fang, X. Dai, and Y. Kawazoe, Phys. Rev. B **92**, 045108 (2015).
[8] K. Mullen, B. Uchoa, and D. T. Glatzhofer, Phys. Rev. Lett. **115**, 026403 (2015).
[9] L. S. Xie, L. M. Schoop, E. M. Seibel, Q. D. Gibson, W. Xie, and R. J. Cava, APL Mater. **3**, 083602 (2015).
[10] G. Bian *et al.*, Nat. Commun. **7**, 10556 (2016).
[11] L. M. Schoop, C. Straßer, A. Topp, V. Duppel, B. V. Lotsch, C. R. Ast, M. N. Ali, S. S. P. Parkin, A. Varykhalov, and D. Marchenko, Nat. Commun. **7**, 11696 (2016).
[12] Y. Okamoto, T. Inohara, A. Yamakage, Y. Yamakawa, and K. Takenaka, J. Phys. Soc. Jpn. **85**, 123701 (2016).
[13] J. Hu, Z. Tang, J. Liu, X. Liu, Y. Zhu, D. Graf, K. Myhro, S. Tran, C. N. Lau, J. Wei, and Z. Mao, Phys. Rev. Lett. **117**, 016602 (2016).
[14] J. Hu, Z. Tang, J. Liu, Y. Zhu, J. Wei, and Z. Mao, Phys. Rev. B **96**, 045127 (2017).
[15] C. Q. Xu, W. Zhou, R. Sankar, X. Z. Xing, Z. X. Shi, Z. D. Han, B. Qian, J. H. Wang, Z. Zhu, J. L. Zhang, A. F. Bangura, N. E. Hussey, and X. Xu, Phys. Rev. Mater. **1**, 064201 (2017).
[16] R. Lou, P. Guo, M. Li, Q. Wang, Z. Liu, S. Sun, C. Li, X. Wu, Z. Wang, Z. Sun, D. Shen, Y. Huang, K. Liu, Z.-Y. Lu, H. Lei, H. Ding, and S. Wang, Quantum Mater. **3**, 43 (2018).
[17] A. Laha, S. Malick, R. Singha, P. Mandal, P. Rambabu, V. Kanchana, and Z. Hossain, Phys. Rev. B **99**, 241102(R) (2019).
[18] Z. Qiu, C. Le, Z. Liao, B. Xu, R. Yang, J. Hu, Y. Dai, and X. Qiu, Phys. Rev. B **100**, 125136 (2019).
[19] C. Sims, M. M. Hosen, H. Aramberri, C.-Y. Huang, G. Dhakal, K. Dimitri, F. Kabir, S. Regmi, X. Zhou, T.-R. Chang, H. Lin, D. Kaczorowski, N. Kioussis, and M. Neupane, arXiv:1906.09642.
[20] T. Nakamura, S. Souma, Z. Wang, K. Yamauchi, D. Takane, H. Oinuma, K. Nakayama, K. Horiba, H. Kumigashira, T. Oguchi, T. Takahashi, Y. Ando, and T. Sato, Phys. Rev. B **99**, 245105 (2019).
[21] J.-W. Rhim and Y. B. Kim, Phys. Rev. B **92**, 045126 (2015).
[22] C. Fang, Y. Chen, H.-Y. Kee, and L. Fu, Phys. Rev. B **92**, 081201(R) (2015).
[23] H. Huang, J. Liu, D. Vanderbilt, and W. Duan, Phys. Rev. B **93**, 201114(R) (2016).
[24] Y.-H. Chan, C.-K. Chiu, M. Y. Chou, and A. P. Schnyder, Phys. Rev. B **93**, 205132 (2016).
[25] A. Yamakage, Y. Yamakawa, Y. Tanaka, and Y. Okamoto, J. Phys. Soc. Jpn. **85**, 013708 (2016).
[26] J.-L. Lu, W. Luo, X.-Y. Li, S.-Q. Yang, J.-X. Cao, X.-G. Gong, and H.-J. Xiang, Chin. Phys. Lett. **34**, 057302 (2017).
[27] Q. Xu, R. Yu, Z. Fang, X. Dai, and H. Weng, Phys. Rev. B **95**, 045136 (2017).
[28] Y. Du, X. Bo, D. Wang, E.-j. Kan, C.-G. Duan, S. Y. Savrasov, and X. Wan, Phys. Rev. B **96**, 235152 (2017).
[29] J. Liu and L. Balents, Phys. Rev. B **95**, 075426 (2017).
[30] L. Oroszlány, B. Dóra, J. Cserti, and A. Cortijo, Phys. Rev. B **97**, 205107 (2018).
[31] A. Martín-Ruiz and A. Cortijo, Phys. Rev. B **98**, 155125 (2018).
[32] Y. Wang, H. Hu, and S. Chen, Phys. Rev. B **98**, 205410 (2018).
[33] A. Lau and C. Ortix, Phys. Rev. Lett. **122**, 186801 (2019).
[34] M. Ezawa, Sci. Rep. **9**, 5286 (2019).
[35] A. A. Burkov, M. D. Hook, and L. Balents, Phys. Rev. B **84**, 235126 (2011).
[36] Y. Chen, Y. Xie, S. A. Yang, H. Pan, F. Zhang, M. L. Cohen, and S. Zhang, Nano Lett. **15**, 6974 (2015).
[37] D. W. Zhang, Y. X. Zhao, R. B. Liu, Z. Y. Xue, S. L. Zhu, and Z. D. Wang, Phys. Rev. A **93**, 043617 (2016).
[38] S. Sur and R. Nandkishore, New J. Phys. **18**, 115006 (2016).
[39] R. Nandkishore, Phys. Rev. B **93**, 020506(R) (2016).
[40] B. Roy, Phys. Rev. B **96**, 041113(R) (2017).
[41] H. Shapourian, Y. Wang, and S. Ryu, Phys. Rev. B **97**, 094508 (2018).
[42] M. A. N. Araújo and L. Li, Phys. Rev. B **98**, 155114 (2018).
[43] S. V. Syzranov and B. Skinner, Phys. Rev. B **96**, 161105(R) (2017).
[44] W. Chen, H.-Z. Lu, and O. Zilberberg, Phys. Rev. Lett. **122**, 196603 (2019).
[45] J. H. Pixley, P. Goswami, and S. Das Sarma, Phys. Rev. Lett. **115**, 076601 (2015).
[46] J. H. Pixley, P. Goswami, and S. Das Sarma, Phys. Rev. B **93**, 085103 (2016).

[47] J. H. Pixley, D. A. Huse, and S. Das Sarma, Phys. Rev. X **6**, 021042 (2016).
[48] M. Buchhold, S. Diehl, and A. Altland, Phys. Rev. B **98**, 205134 (2018).
[49] B. Roy, R.-J. Slager, and V. Juričić, Phys. Rev. X **8**, 031076 (2018).
[50] K. Kobayashi, T. Ohtsuki, K. I. Imura, and I. F. Herbut, Phys. Rev. Lett. **112**, 016402 (2014).
[51] For Gaussian distributed disorder, rare region effects were proposed to add a finite spectral weight at zero energy, causing an avoided quantum critical point [47]. However, these effects were shown to add finite spectral weight only in the neighborhood of $E = 0$, not affecting the finite-disorder semimetallic phase [48].
[52] Y. Huh, E.-G. Moon, and Y. B. Kim, Phys. Rev. B **93**, 035138 (2016).
[53] Y. Wang and R. M. Nandkishore, Phys. Rev. B **96**, 115130 (2017).
[54] S. P. Mukherjee and J. P. Carbotte, Phys. Rev. B **95**, 214203 (2017).
[55] M. Andelković, S. M. João, L. Covaci, T. Rappoport, J. M. P. Lopes, and A. Ferreira, quantum-kite/kite: Pre-release" (2019).
[56] S. M. João and J. M. V. P. Lopes, J. Phys. Condens. Matter **32**, 125901 (2020).
[57] S. M. João *et al.*, R. Soc. Open Sci. **7**, 191809 (2020).
[58] J. H. Pixley, J. H. Wilson, D. A. Huse, and S. Gopalakrishnan, Phys. Rev. Lett. **120**, 207604 (2018).
[59] Y. Fu, E. J. König, J. H. Wilson, Y.-Z. Chou, and J. H. Pixley, arXiv:1809.04604.
[60] M. Janssen, Int. J. Mod. Phys. B **08**, 943 (1994).
[61] See Supplemental Material at http://link.aps.org/supplemental/10.1103/PhysRevLett.124.136405 for additional results obtained with ED, including the critical point computation, scaling analysis, and level statistics; additional details on the computation of the critical point of the 1D–3D diffusive transition; characterization of large disorder metal-insulator transition; additional results on wave function properties; and discussion on resolution issues for small disorder, which includes Refs. [50,60,62–65].
[62] K. H. Hoffmann and M. Schreiber, *Computational Statistical Physics* (Springer Berlin Heidelberg, Berlin, Heidelberg, 2002).
[63] Y. Y. Atas, E. Bogomolny, O. Giraud, and G. Roux, Phys. Rev. Lett. **110**, 084101 (2013).
[64] A. MacKinnon and B. Kramer, Phys. Rev. Lett. **47**, 1546 (1981).
[65] A. MacKinnon and B. Kramer, Z. Phys. B **53**, 1 (1983).
[66] Y. Ominato and M. Koshino, Phys. Rev. B **89**, 054202 (2014).
[67] All the even system sizes within the L intervals shown in the legend of Fig. 3(a) are used to extract τ_k.
[68] As we were only interested in the scaling of Γ with L, in the plots we use $\Gamma = 1/(\mathcal{I}_k L^3)$.
[69] F. J. Wegner, Z. Phys. B **25**, 327 (1976).
[70] K. Slevin and T. Ohtsuki, Phys. Rev. Lett. **78**, 4083 (1997).
[71] K. Slevin and T. Ohtsuki, Phys. Rev. Lett. **82**, 382 (1999).
[72] Y. Asada, K. Slevin, and T. Ohtsuki, J. Phys. Soc. Jpn. **74**, 238 (2005).
[73] M. Gonçalves, P. Ribeiro, E. V. Castro, and M. A. N. Araújo (to be published).
[74] R.-J. Slager, V. Juričić, and B. Roy, Phys. Rev. B **96**, 201401 (R) (2017).
[75] R. Nandkishore, D. A. Huse, and S. L. Sondhi, Phys. Rev. B **89**, 245110 (2014).
[76] J. H. Wilson, J. H. Pixley, D. A. Huse, G. Refael, and S. Das Sarma, Phys. Rev. B **97**, 235108 (2018).